Gondwana Research 23 (2013) 25–38

Contents lists available at SciVerse ScienceDirect

Gondwana Research

journal homepage: www.elsevier.com/locate/gr

Distinct variations of crustal shear wave velocity structure and radial anisotropy beneath the North China Craton and tectonic implications

Cheng Cheng [a,1], Ling Chen [a,*], Huajian Yao [b], Mingming Jiang [a], Bingyu Wang [a]

[a] State Key Laboratory of Lithospheric Evolution, Institute of Geology and Geophysics, Chinese Academy of Sciences, China
[b] IGPP, Scripps Institute of Oceanography, UCSD, La Jolla, CA, United States

ARTICLE INFO

Article history:
Received 30 September 2011
Received in revised form 24 February 2012
Accepted 26 February 2012
Available online 5 March 2012

Keywords:
Ambient noise tomography
North China Craton
Crustal shear velocity
Radial anisotropy
Crustal deformation

ABSTRACT

This study presents the crustal shear wave velocity structure and radial anisotropy along two linear seismic arrays across the North China Craton (NCC) from ambient noise tomography. About a half to one year long ambient noise data from 87 stations were used for obtaining the inter-station surface wave empirical Green's functions (EGFs) from cross-correlation. Rayleigh and Love dispersion curves within the period band 5–30 s were measured from the EGFs of the vertical and transverse components, respectively. These dispersion data were then used to determine the crustal shear wave velocity structure (V_{SV} and V_{SH}) and radial anisotropy ($2(V_{SH}-V_{SV})/(V_{SH}+V_{SV})$) from point-wise linear inversion with constraints from receiver function analysis. Our results reveal substantial structural variations among different parts of the NCC. The Bohai Bay Basin in the eastern NCC is underlain by a thin crust (~30 km) with relatively low velocities (particularly V_{SV}) and large positive radial anisotropy in the middle to lower crust. Such a crustal structure is no longer of a cratonic type and may have resulted from the widespread tectonic extension and intensive magmatism in this region since late Mesozoic. Beneath the Ordos Basin in the western NCC, the crust is relatively thicker (≥40 km) and well stratified, and presents a large-scale low velocity zone in the middle to lower crust and overall weak radial anisotropy except for a localized lower crust anomaly. The overall structural features of this region resemble those of typical Precambrian shields, in agreement with the long-term stability of the region. The crustal structure under the Trans North China Orogen (TNCO, central NCC) is more complicated and characterized by smaller scale velocity variations, strong positive radial anisotropy in the middle crust and rapid change to weak-to-negative anisotropy in the lower crust. These features may reflect complex deformations and crust–mantle interactions, probably associated with tectonic extension and magmatic underplating during the Mesozoic to Cenozoic evolution of the region. Our structural images in combination with previous seismic, geological and geochemical observations suggest that the Phanerozoic lithospheric reactivation and destruction processes may have affected the crust (especially the middle and lower crust) of the eastern NCC, and the effect probably extended to the TNCO, but may have minor influence on the crust of the western part of the craton.

1. Introduction

The North China Craton (NCC), preserving >3.0 Ga crustal rocks, is one of the oldest cratons on the earth (e.g., Liu et al., 1992; Zheng et al., 2004; Zhai and Santosh, 2011). However, from late Mesozoic to Cenozoic the NCC experienced significant tectonic reactivation and destruction during which the old, cold, thick and refractory lithospheric mantle in its eastern part was replaced by a young, hot, thin and relatively fertile mantle accompanied by voluminous magmatism, widespread lithospheric extension and development of large sedimentary basins (Griffin et al., 1998; Zhao et al., 2001; Xu et al., 2004; Menzies et al., 2007). Geochemically, the eastern NCC was proven to have suffered much stronger destruction than any other cratons and has become the most striking example of cratonic destruction in the world (e.g., Carlson et al., 2005; Wu et al., 2008; Zhang et al., 2011a). On the other hand, the central and western NCC remains tectonically stable despite the occurrence of sporadic volcanism and localized lithospheric extension in mechanically weak zones surrounding the cratonic core of the region (Zhang et al., 2003; Xu et al., 2004). This unique feature makes the NCC the best natural laboratory to study the formation, stability and destruction of old cratons.

A lot of geophysical investigations have focused on the deep structure of the NCC. Recent seismic imaging results (e.g., Chen et al., 2008, 2009; Zhao et al., 2008, 2009; Chen, 2010; Bao et al., 2011) have revealed significant regional variations in the lithospheric structure of this region, from the widespread thinned lithosphere (60–100 km) in the eastern NCC to the coexistence of both thinned (<100 km) and well-preserved thicker lithosphere (>200 km) in the central and western NCC. The lithospheric structure variations are closely correlated with the contrasting

* Corresponding author. Tel.: +86 10 82998416; fax: +86 10 62010846.
E-mail addresses: cchengster@berkeley.edu (C. Cheng), lchen@mail.iggcas.ac.cn (L. Chen).
[1] Now at University of California-Berkeley, Department of Earth and Planetary Science.

1342-937X/$ – see front matter © 2012 International Association for Gondwana Research. Published by Elsevier B.V. All rights reserved.
doi:10.1016/j.gr.2012.02.014

geologic features and tectonics between the eastern and central to western NCC (Xu, 2007; Chen, 2010). These observations offer compelling support for the speculation that fundamental lithospheric destruction mainly occurred in the eastern NCC, whereas the cratonic mantle root underneath the central and western NCC was only locally modified (Zhu et al., 2011).

An issue still under debate is whether or not and to what extent the Mesozoic to Cenozoic cratonic destruction and modifications have changed the crust of the NCC. One opinion suggests that these processes may have only involved the lithospheric mantle with the overlying crust largely undisturbed (Menzies et al., 1993; Xu et al., 1995; Zheng et al., 2001), while another opinion insists that the processes have significantly affected the crust (Gao et al., 2004; Wu et al., 2005; Deng et al., 2007), but it is still far from reaching a consensus that by what means and to what degree the crust has been affected (e.g., Jiang and Guo, 2010). Obviously, detailed information about the structure and deformation of the crust is essential to gain further insight into this issue.

Based on the new seismic data recently collected by dense broadband arrays and deep seismic sounding, fine-scale crustal structure images have been obtained for various parts of the NCC (e.g., Li et al., 2006; Zheng et al., 2008, 2009b; Teng et al., 2010; Li et al., 2011; Tian et al., 2011; Wei et al., 2011), revealing substantial structural variations of the region. In particular, a generally slow and thin crust (mostly <35 km) was imaged under the eastern NCC, whereas a thicker (~40 up to 60 km) and structurally complex crust was proposed to be characteristic of the central and western NCC. These remarkable changes in the crustal structure appear to be correlated with the distinct regional variations of lithospheric structure and surface geology, reflecting complex crustal tectonics and evolution of the craton. However, discrepancies in the derived structural features of the crust, such as velocity distributions and crustal thickness, still exist in some regions of the craton in the results from different imaging methods and/or subsets of data (e.g., Wei et al., 2011), for instance, from active- (e.g., Teng et al., 2010; Li et al., 2011; Zhang et al., 2011b and references therein) and passive-source data (e.g., Zheng et al., 2009b; Zhu and Zheng, 2009; Tian et al., 2011). This results in larger uncertainties in the crustal structure and therefore a less direct link between seismic velocity structure and regional geology and tectonics. In addition, crustal anisotropy, a feature primarily associated with crustal deformation resulting from tectonic processes, remains poorly constrained especially in the middle to lower crust for many regions of the NCC, due largely to the difficulties to observe seismically based on traditional methods (Meissner et al., 2006). In these regards, more reliable observations of both isotropic and anisotropic crustal structure are required to decipher the detailed structure and deformation of the crust and to understand the crust–mantle interaction during the Mesozoic to Cenozoic reactivation and destruction of the NCC.

Surface waves have been used to study the crust and upper mantle structure on both regional and global scale. Surface wave tomography can provide constraints on the absolute values and smooth variations of shear wave velocities at depth, and therefore is complementary to other imaging techniques (e.g., receiver function imaging or body wave tomography) that mainly give information about the structures of interfaces or velocity perturbations relative to a reference model. However, it is difficult to obtain reliable constraints on crustal structure from earthquake-based surface wave dispersions because teleseismic surface waves at short periods (e.g., T<25 s) are usually attenuated and scattered due to strong crustal heterogeneity. Besides, sparse and uneven distributions of earthquake sources and uncertainties of earthquake locations also limit the resolution and accuracy of traditional surface wave tomography. Ambient noise tomography, based on cross-correlation of the ambient noise field between pairs of stations, overcomes the above limitations of earthquake-based methods (e.g., Shapiro et al., 2005; Yao et al., 2006). Recently, this method has been widely used in imaging crustal structure (Yang et al., 2007b; Bensen et al., 2008; Yao et al., 2008; Lin et al., 2008a) because of its unique ability to obtain surface wave dispersion curves at short to intermediate periods (5~30s). The dispersion characteristics (phase or group velocities) of Rayleigh and Love waves at these periods provide constraints on the velocities of vertically and horizontally polarized shear waves, respectively, and therefore on the anisotropy of the crustal and uppermost mantle independent of earthquakes or man-made explosions, which expands the depth range of reliable surface wave tomography to the crust.

In this study, detailed images of crustal shear wave velocity structure along two linear seismic arrays across the NCC are constructed by inverting the phase velocity dispersion curves of both Rayleigh and Love waves obtained from ambient noise interferometry. Compared with previous seismic studies of the study region (e.g., Zheng et al., 2009b; Wei et al., 2011), this paper mainly focuses on larger scale E–W variations of the crustal structure including radial anisotropy constrained from the differences between the Rayleigh and Love wave inversion results. The implications of our images on the crustal deformation and destruction and modification of the NCC are discussed from regional tectonics point of view.

2. Data and ambient noise cross-correlations

The continuous three-component seismic data used in this study come from two linear temporary broadband seismic arrays NCISP-II and NCISP-IV (two subprojects of NCISP, North China Interior Structure Project) deployed by the Institute of Geology and Geophysics, Chinese Academy of Sciences. As illustrated in Fig. 1, these two arrays start from the interior of the Bohai Bay Basin in the east, cross the Taihang Mountains in the middle, and end at the western portion of the Ordos Basin in the west, traversing all the three constituent parts of the NCC. The NCISP-II array trends NW–SE, roughly perpendicular to the boundary of the eastern and central NCC but sub-parallel to the dominant regional extension direction (NW–SE to NWW–SEE) in the Late Mesozoic to Early Cenozoic (e.g., Ren et al., 2002; Lin et al., 2008b). The NCISP-IV array is connected with the NCISP-II array near the boundary between the central and western NCC and goes along an E–W direction in the northern part of the western NCC (Fig. 1). Here we considered a total of 87 stations from the arrays with most of the interstation distances on the order of ~10 km. We used about one-year (September 2005–August 2006) continuous data recorded at the 50 NCISP-IV stations and six months (September 2001–February 2002) of data at the 37 NCISP-II stations for ambient noise analysis. According to the previous studies on the time dependence of the empirical Green's functions of surface waves derived from ambient noise (e.g., Shapiro et al., 2005; Yao et al., 2006; Yao and van der Hilst, 2009), these durations of data appear to be sufficiently long for reliable measurements of phase velocities at relatively short periods (e.g., ≤30 s in this study). Since the operation time periods of the two arrays are different, we analyzed the two sets of data separately.

We processed the data similarly to the standard procedure of noise cross-correlation proposed previously (Shapiro et al., 2004; Yao et al., 2006; Bensen et al., 2007). The continuous data were first cut into one-day long segments and decimated to 10 samples per second, and then were filtered to the 0.5–40 s period band. In order to reduce the influences of earthquakes and non-stationary signals, we first muted the one-day data if an earthquake of magnitude larger than 6.5 occurred during that day. Then we performed both temporal normalization using running-absolute-mean method (Bensen et al., 2007) and spectral whitening over the same frequency band as for data filtering. Since the seismometers for each array are of the same type, removal of the instrument response is not necessary and so was not performed. Next, the processed one-day-long traces were cross-correlated between all station-pairs. Finally for each station-pair, we stacked all available daily cross-correlations of vertical components and took the negative time derivatives to produce the Rayleigh wave

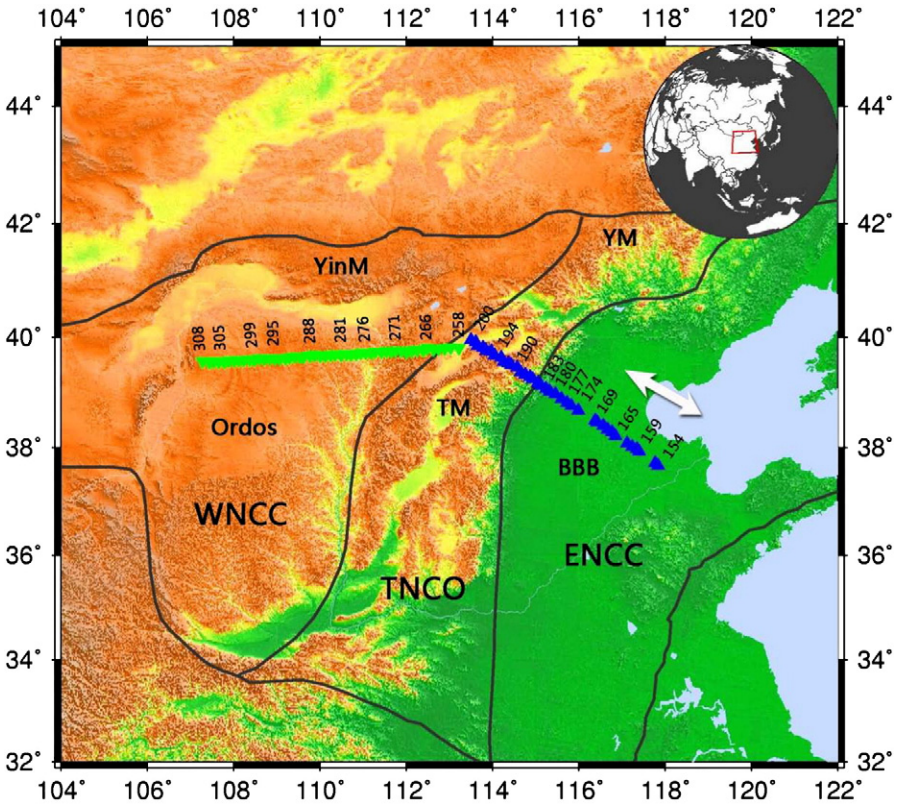

Fig. 1. Study region and locations of broadband seismic stations. Blue triangles stand for the 37 NCISP-II stations and green inverted triangles for the 50 NCISP-IV stations. Some station numbers are marked alongside the corresponding stations. Black solid lines mark the boundaries of the North China Craton (NCC) and its three constituent parts: the western NCC (WNCC), the Trans-North China Orogen (TNCO, the central NCC) and the eastern NCC (ENCC). Double-headed arrow gives the possible regional extension direction during the Late Mesozoic to Early Cenozoic. BBB: Bohai Bay Basin, TM: Taihang Mountains, YM: Yan Mountains, YinM: Yin Mountains.

Empirical Green's functions (EGFs), and those of transverse components to produce the Love wave EGFs (e.g., Lin et al., 2008a). An example of the record section of vertical component EGFs between station 258 and other stations of the NCISP-IV array is presented in Fig. 2a, which shows clear Rayleigh wave signals with an approximate moveout of ~3.13 km/s.

3. Phase velocity dispersion and tomography

3.1. Dispersion measurements

The phase velocity dispersion curves were determined from the EGFs based on a far-field representation of the surface-wave Green's function and an image transformation technique, following the procedure described previously (Fig. 2, Yao et al., 2005, 2006). The causal and acausal parts were averaged to create the symmetric components of cross-correlations (Yang et al., 2007b) for the dispersion analysis. We emphasize that the surface wave phase velocities were measured at a given period from the calculated velocity-period image (Fig. 2c) only when the following two prerequisites were satisfied: 1) the distance between the pair of stations must be at least three wavelengths in order to satisfy the far-field approximation; 2) the signal-to-noise ratio (SNR) of the corresponding EGF is sufficiently high (>5, Fig. 2b and c). Here the SNR is defined as the ratio of the maximum amplitude of the signal window (determined by a group-velocity window, e.g., 2.5–5 km/s) and the mean envelope amplitude of the 150 s long noise window right after the signal window (Fig. 2b) at around the considered period. A narrow frequency band of 0.4 s was adopted to filter the EGFs at each central period in the calculation of the velocity-period image and envelope amplitudes in both the signal and noise windows.

We measured the phase velocity dispersion curves for all possible station pairs along the two seismic arrays. Unreasonable dispersion curves that are obviously different from the majority were removed by careful visual inspection. Due largely to the different durations of the raw data used that affect the quality and SNR of the recovered surface-wave EGFs, the NCISP-IV data yielded many more Rayleigh and Love wave dispersion curves with slightly broader period bands than the NCISP-II data did (Table 1). According to the topography and geological features of the study region, we classified the station pairs and thus the dispersion curves into basin–basin, basin–mountain, and mountain–mountain groups for both arrays (Fig. 3a and b). These three groups of dispersion curves are distinguishable, especially in the short period band at which the surface waves are much sensitive to the shallow velocity structures of thick sedimentary basins and mountain areas. The discrepancies of different groups of dispersion curves can be seen more clearly by comparing the average phase velocities of these groups (Fig. 3c). Generally, phase velocities of the basin–basin group are significantly lower at <20 s but increase the fastest with period than the other two groups. In contrast, the mountain–mountain group has the highest phase velocities at shorter periods but relatively low phase velocities at longer periods, exhibiting the slowest increase in phase velocities with period. The basin–mountain group shows intermediate features among the three. For all the groups, the Love wave phase velocities vary with period at similar rates to their Rayleigh wave counterparts at >20 s but decrease more rapidly toward shorter periods, especially for the basin–basin group (Fig. 3c). This observation probably reflects the effects of slow thick sediments or the presence of radial anisotropy, or both.

To estimate the uncertainty of the phase velocity measurements and robustness of the above mentioned features, we constructed the EGFs and then measured the phase velocities using different months

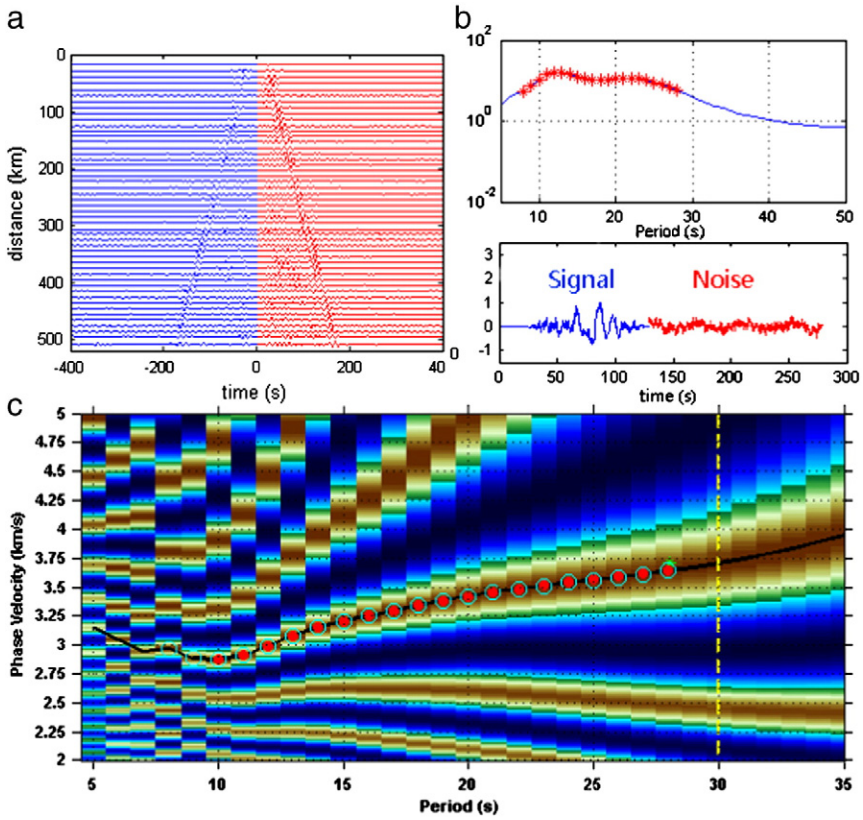

Fig. 2. (a) Rayleigh wave empirical Green functions (EGFs) between station 258 and other stations along the NCISP-IV array. Traces are band-pass filtered in the period band 5–35 s, windowed with group velocity >2.5 km/s and sorted according to the interstation distances. (b) Signal-to-noise ratios (SNRs) (top panel) of the EGF for the station pair 258–280 (trace in the bottom panel) with red stars for SNRs larger than 5. The blue part in the bottom panel stands for the Rayleigh wave signal window and red part for the noise window considered in the calculation of the SNRs. (c) Phase velocity dispersion measurement for the station pair 258–280 based on the image transformation technique (Yao et al., 2005; 2006). Yellow line represents the cutoff period at which the interstation distance reaches three wavelengths. Cyan circles mark the velocity-period coordinates where the SNRs are larger than 5. Red dots in (c) superposed on the black line are the phase velocities finally determined from the EGF.

of data and compared them with those obtained from all available data (Fig. 3). We found that the deviations of the monthly dispersion curves for both individual station pairs and the groups are generally small (<1%). These results indicate that the EGFs calculated can give reliable phase velocity measurements in the period band considered in this study.

3.2. Phase velocity tomography

We applied a damped least-square tomography technique (Yang, 1996) to invert the measured inter-station phase velocity dispersion curves from each array (NCISP-II or NCISP-IV) for phase velocities along that array between all the neighboring stations. In order to improve the reliability of the inversion results, we carried out tomographic inversion twice to account for possible large errors in the phase velocity measurements. Bad measurements with unreasonably high travel-time misfits (>3 s in this study) after the first time tomography were discarded in the second time tomography, similarly to that implemented in the previous studies of ambient noise tomography for some other regions (e.g., Yang et al., 2007b, 2010).

Table 1
Period bands and numbers of the dispersion curves retrieved in this study.

	NCISP-II	NCISP-IV
Rayleigh	8–30 s, 345 curves	5–30 s, 894 curves
Love	10–25 s, 260 curves	7–27 s, 794 curves

The final results of phase velocity tomography along the two seismic arrays are shown in Fig. 4. The most notable feature of the images is perhaps the good correlation between phase velocities at shorter periods and large-scale geological structures of the study region. At periods below 15 s, phase velocities are dominantly sensitive to shear wave velocities in the upper crust. Since seismic velocities of sediments are much slower than those of crystalline rocks, major sedimentary basins, including the Bohai Bay Basin in the east and the Ordos Basin in the west, are well delineated with low phase velocities, and the Taihang Mountains in between with relatively high phase velocities. Above 15 s, phase velocity contrasts between the basins and mountains are gradually reduced, in accordance with the decrease of structural differences among these areas at larger depths. At longer periods (20–30 s), lateral variations in phase velocities persist but are more obvious for Love waves (Fig. 4b) than for Rayleigh waves (Fig. 4a), although the variation magnitudes of both are further reduced.

4. Shear wave velocity structure

4.1. Inversion scheme

More detailed interpretation of the observed phase velocity variations requires inversion for the shear wave velocity structure of the crust and uppermost mantle. We carried out individual 1D inversion of the Rayleigh and Love phase velocity dispersion curves for the shear wave velocity structure beneath each pair of neighboring stations, using a damped least-square inversion scheme developed by Herrmann and Ammon (2004). Given that the phase velocity data at the periods of 8–30 s

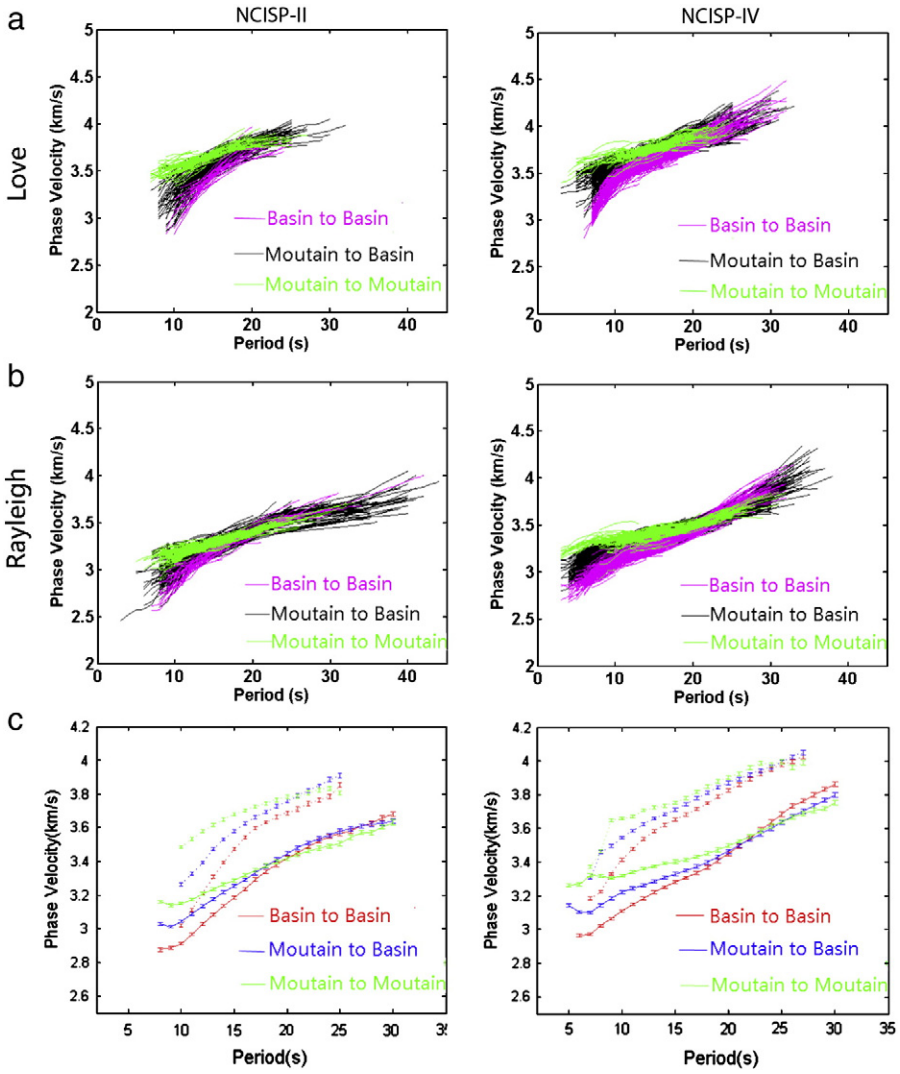

Fig. 3. Phase velocity dispersion curves of Love (a) and Rayleigh waves (b) for all the station pairs in the two arrays. Pink lines represent dispersion curves for basin–basin station pairs, black lines for mountain–basin station pairs, and green lines for mountain–mountain station pairs. (c) Average phase velocity dispersion curves and average standard errors for the different types of station pairs from the EGF analysis. Solid and dotted lines are for Rayleigh and Love waves, respectively.

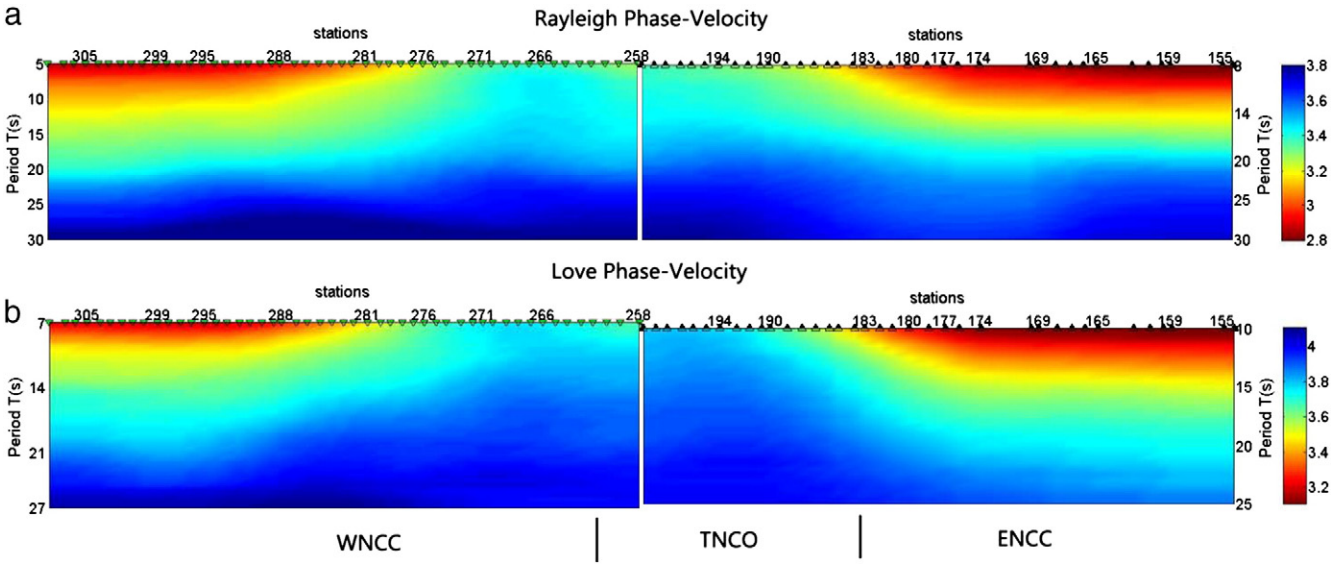

Fig. 4. Rayleigh (a) and Love (b) phase velocity cross-section along the two seismic arrays.

(Table 1) can best constrain the shear wave velocities in the crust, in this study we targeted our inversion results in the crust. A priori structural information along the two arrays derived from previous receiver function studies (Zheng et al., 2009b; Wei et al., 2011) was incorporated into our initial models, including the Moho depths, average Vp/Vs ratios of the crust, and the top 4-km sedimentary layer with very low velocities in the Bohai Bay Basin. In each inversion run, we fixed the Moho depth and Vp/Vs ratio and inverted for the best-fitting shear wave velocities in the crust (parameterized by a stack of 2-km thick layers) and uppermost mantle (a uniform layer between Moho and 60-km depth). Since the Moho depths beneath the Ordos Basin obtained in the two previous studies are generally different from each other (Wei et al.'s results are deeper than Zheng et al.'s by up to 6 km), we tested the Moho depths from both studies. To further assess the effects of the initial model on the inversion result, we also adopted various other initial models (e.g., without the top 4-km low-velocity sedimentary layer in the Bohai Bay Basin, changing the near surface velocities in the Ordos Basin, using different Vp/Vs ratios, etc.) and compared the inverted shear velocities thoroughly.

Our results show that using different initial models yielded very similar structural features in the inverted models and comparable misfit between the synthetic and observed phase velocity dispersion curves, especially for the middle and lower crust (Fig. 5), suggesting relatively minor effects of the choice of initial models on the inversion results of our targeted crustal structure. In particular, we found that the choice of initial models with large velocity differences of more than 30% in the top several kilometers and a change of the Moho depth by up to 6 km does not significantly affect the inverted crustal structure (except at around the Moho depth in the later case, Fig. 5e). These testing results demonstrate the robustness of our inversion results. We chose the inversion results by incorporating a priori structural information (with the Moho depth from Zheng et al., 2009b) for later interpretation.

In the linear array case of our study, the inverted shear wave velocities mainly represent the velocities of shear waves propagating along the direction of the arrays but with different polarization directions. The velocity models constructed from Rayleigh waves correspond to vertically polarized shear waves (V_{SV}) and those from Love waves to horizontally polarized shear waves (V_{SH}) with polarization direction perpendicular to the array (roughly N–S for the NCISP-IV array and NE–SW for the NCISP-II array). The inverted models derived for individual pair of neighboring stations were compiled to form the final V_{SV} and V_{SH} images along the two arrays (Fig. 6a and b). A radial anisotropy image (Fig. 6c) was also constructed by considering the discrepancies between the V_{SV} and V_{SH} structure. Here we quantify radial anisotropy as $2*(V_{SH}-V_{SV})/(V_{SH}+V_{SV})$, similarly to the percent anisotropy defined previously (Savage, 1998).

4.2. Inversion results

All the images present significant structural variations from east to west in the study region. Very low velocities appear at shallow depth in both the Bohai Bay Basin and the Ordos Basin, suggesting that the slow sedimentary structures are well resolved by ambient noise analysis. Beneath the sediments, both basins are dominated by sub-horizontal structure with different crustal velocities, thickness and anisotropy. The Bohai Bay Basin in the eastern NCC exhibits relatively low velocities (with an average V_{SV} of about 3.6 km/s) and strong positive radial anisotropy ($V_{SH}>V_{SV}$, 10%–15%) in the middle to lower crust. Together with the low topography on the surface and a thin crust about 30 km, these features are typical for tectonically active continental regions such as rift zones but never for a stable craton.

In contrast, the Ordos Basin in the western NCC is underlain by a well stratified crust with a thickness of typical Precambrian shields (~40–45 km). The imaged V_{SH} and V_{SV} structures show generally similar variation patterns, which results in an overall weak radial anisotropy

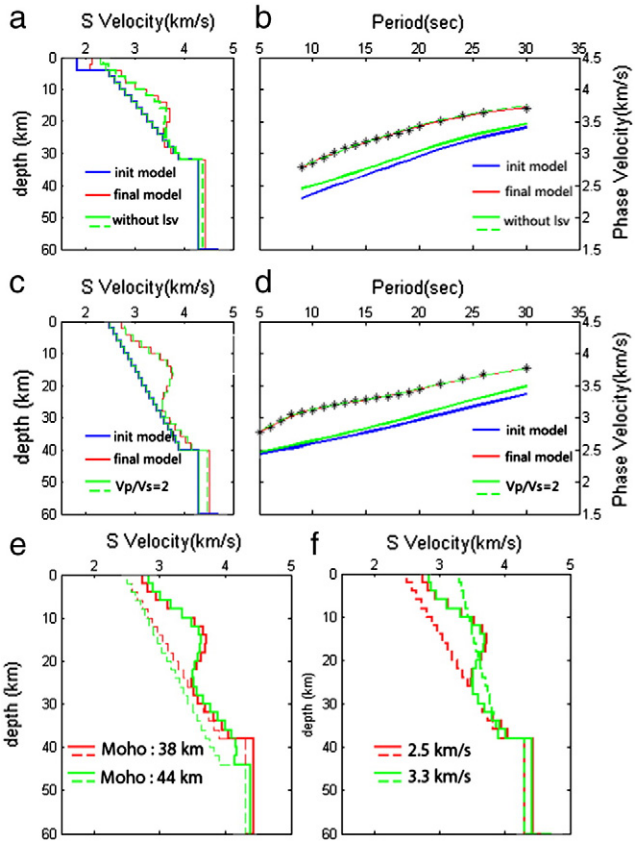

Fig. 5. Shear-wave velocity inversion results for station pairs 160–161 (a, b), 294–295 (c, d) and 307–308 (e, f), respectively. For each station pair, different initial models were considered in the inversion: with (blue and red lines) and without (green and dashed green lines) the top 4-km low sedimentary velocities (lsv) (Zheng et al., 2009b) for 160–161 (a, b), using the average crustal Vp/Vs ratio of 1.78 from Wei et al. (2011) (blue and red lines) and an arbitrarily selected value of 2.0 (green and dashed lines) for 294–295 (c, d), adopting different Moho depths, 38 km (Zheng et al., 2009b) and 44 km (Wei et al., 2011) (e) and different near surface velocities, 2.5 km/s and 3.3 km/s (f), but a same lowermost crustal velocity of 3.9 km/s for 307–308. Black stars and lines in (b) and (d) represent the measured and calculated phase velocities, respectively. In (a–d), solid and dashed green lines are the initial and inverted models, respectively. In (e) and (f), solid lines represent the inverted models and dashed lines the initial models.

of the region. However, apparent positive radial anisotropy of up to 10% is found locally in the lower crust (Fig. 6c), corresponding to the region with anomalously high velocities and an increase in the crustal thickness under the central to eastern Ordos (Fig. 6, Zheng et al., 2009b; Wei et al., 2011).

Another interesting feature of the Ordos region is the presence of a large-scale low velocity zone (LVZ) in the middle to lower crust (~3.4–3.7 km/s, Fig. 6a and b), which is more obvious in the V_{SV} image (Fig. 6a). The existence of the LVZ was verified based on the observations from a number of tests, as exemplified in Fig. 7. (1) The LVZ is always visible no matter what initial models were used in the inversion (see Fig. 7a for examples with or without a Moho discontinuity adopted in the initial model). (2) Despite the uncertainties of the absolute shear velocities, the LVZ well appears in the average inverted model obtained by trial and error (adding 1% random noise to the observed dispersion data, conducting inversion and repeating this process 100 times, see Fig. 7b). This indicates that the LVZ is indeed a robust feature. (3) Without the LVZ in the middle to lower crust results in an obvious increase in phase velocities, especially at 12–25 s (even considering the uncertainties of the phase velocity measurements) and a pattern of variation with period that deviates much from the observations (compare the blue and green lines with the red lines and dots in Fig. 7a). (4) Finally,

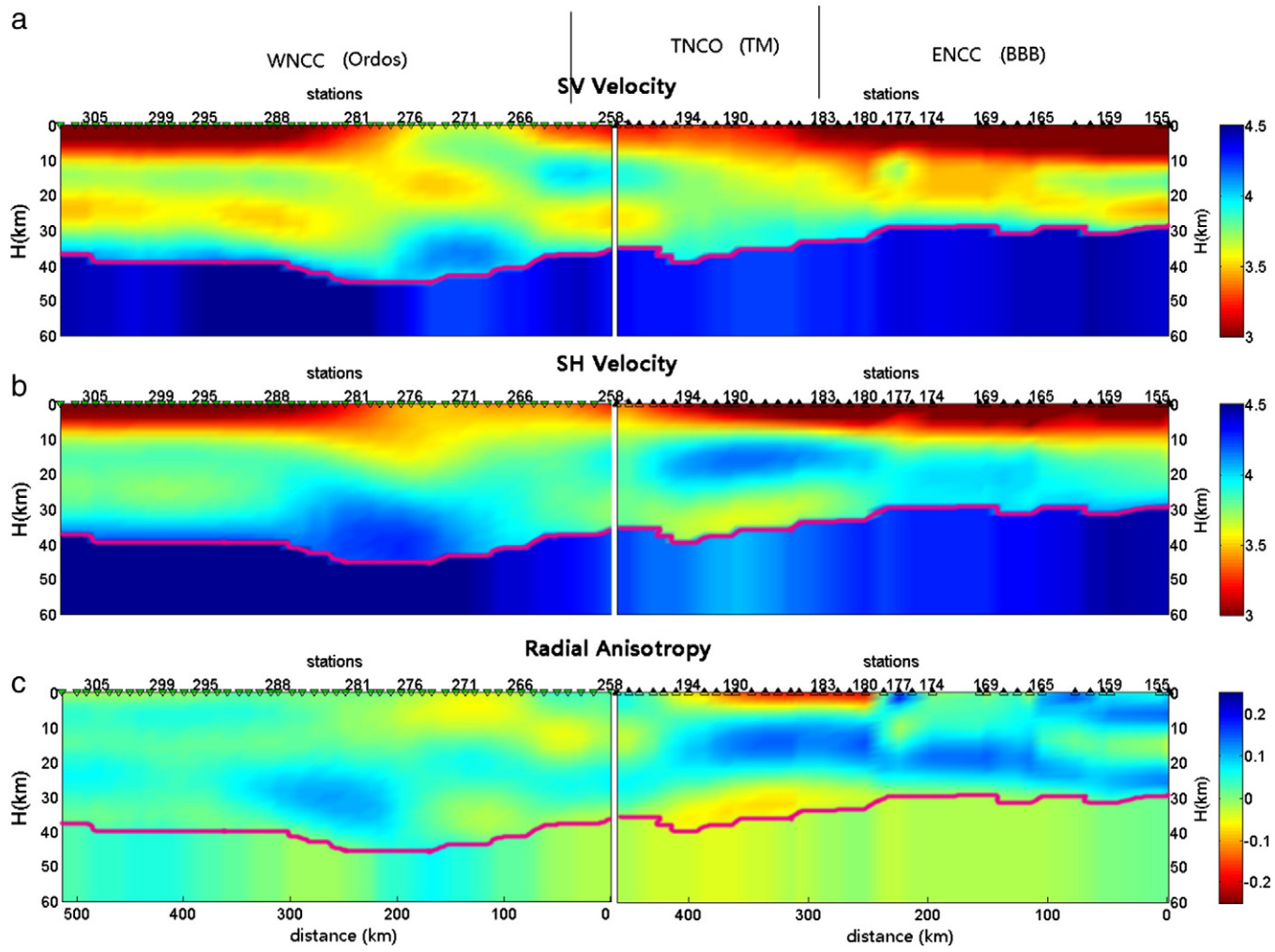

Fig. 6. (a) V_{SV} image obtained by inverting the Rayleigh wave phase velocities from each array. (b) V_{SH} image constructed from inversion of the Love wave phase velocities. (c) Radial anisotropy image along the two arrays with positive values (in blue) for $V_{SH}>V_{SV}$ and negative values (in red) for $V_{SV}<V_{SH}$. The reference Moho depth (from Zheng et al., 2009b) in the inversion is shown as a purple line in each panel. The main tectonic units and boundaries are labeled on the top of the figure.

besides the velocity models inverted from tomographically obtained local dispersion curves, those directly from inter-station dispersion measurements also confirm the existence of a similar LVZ beneath the Ordos Basin, with little dependence on the initial model (Fig. 7c). Our testing results suggest that along the NCISP-IV array, the LVZ exists in a broad region from the eastern part of the Ordos (stations 271–276) all the way to its western edge (stations 305–308, Figs. 6a and 7b).

Previous receiver function studies also imaged the LVZ in the crust beneath the NCISP-IV array but with different lateral extents (Fig. 8, Zheng et al., 2009b; Chen et al., 2009). One study from waveform inversion of receiver functions suggests that the LVZ inclines to the west beneath the eastern to middle part of the Ordos region, but disappears under its western part (L1 in Fig. 8a, Zheng et al., 2009b); whereas the other presents a wave-equation receiver function migration image in which a strong negative signal (the upper interface of the LVZ) can be continuously traced to the western boundary of the Ordos (Fig. 8b, Chen et al., 2009). A latest P wave free surface reverberation study (Chen et al., in preparation) also reveals an interface of the same nature and depths to that imaged by receiver function migration (Fig. 8b). Our surface wave tomography images agree with both these two studies pretty well, which confirms that the LVZ is present under the entire Ordos Basin along the NCISP-IV array. Detailed analysis on all these results further suggests that the LVZ has a fairly small dip to the west (mostly <5°), especially beneath the western Ordos (~1°).

The crustal structure of the TNCO (the central part of the NCC) is much different from that of both the eastern and western NCC. The Taihang Mountain region in the major part of the TNCO is characterized by opposite variations of V_{SH} and V_{SV} with depth (compare Fig. 6a with b), which gives rise to strong positive and weak-to-negative radial anisotropy in the middle and lower crust, respectively (Fig. 6c). While the middle crust positive anisotropy shows a good continuity from that in the middle to lower crust of the eastern NCC, the change to weak-to-negative radial anisotropy in the lower crust is rather rapid and distinct over the study region. The western margin of the TNCO (connection area between the two arrays) shows a high-velocity anomaly in the middle crust underlain by a low-velocity body (more significant in the V_{SV} image in Fig. 6a). The low velocity body could be the LVZ "L2" imaged previously from receiver function waveform inversion (Fig. 8a, Zheng et al., 2009b), but here it appears not to extend too far into the western NCC, more consistent with the receiver function migration image (Fig. 8b, Chen et al., 2009). The radial anisotropy of the area is weak, analogous to the western NCC (Fig. 6c).

We also conducted various tests to testify the reliability of our imaging result in the TNCO, especially the variations of radial anisotropy with depth. For instance, for each neighboring station pair we iteratively adopted the average velocity model from the V_{SH} and V_{SV} inversion results as the initial model and re-invert the Rayleigh and Love phase velocity dispersion curves. The resulting velocity models (with examples

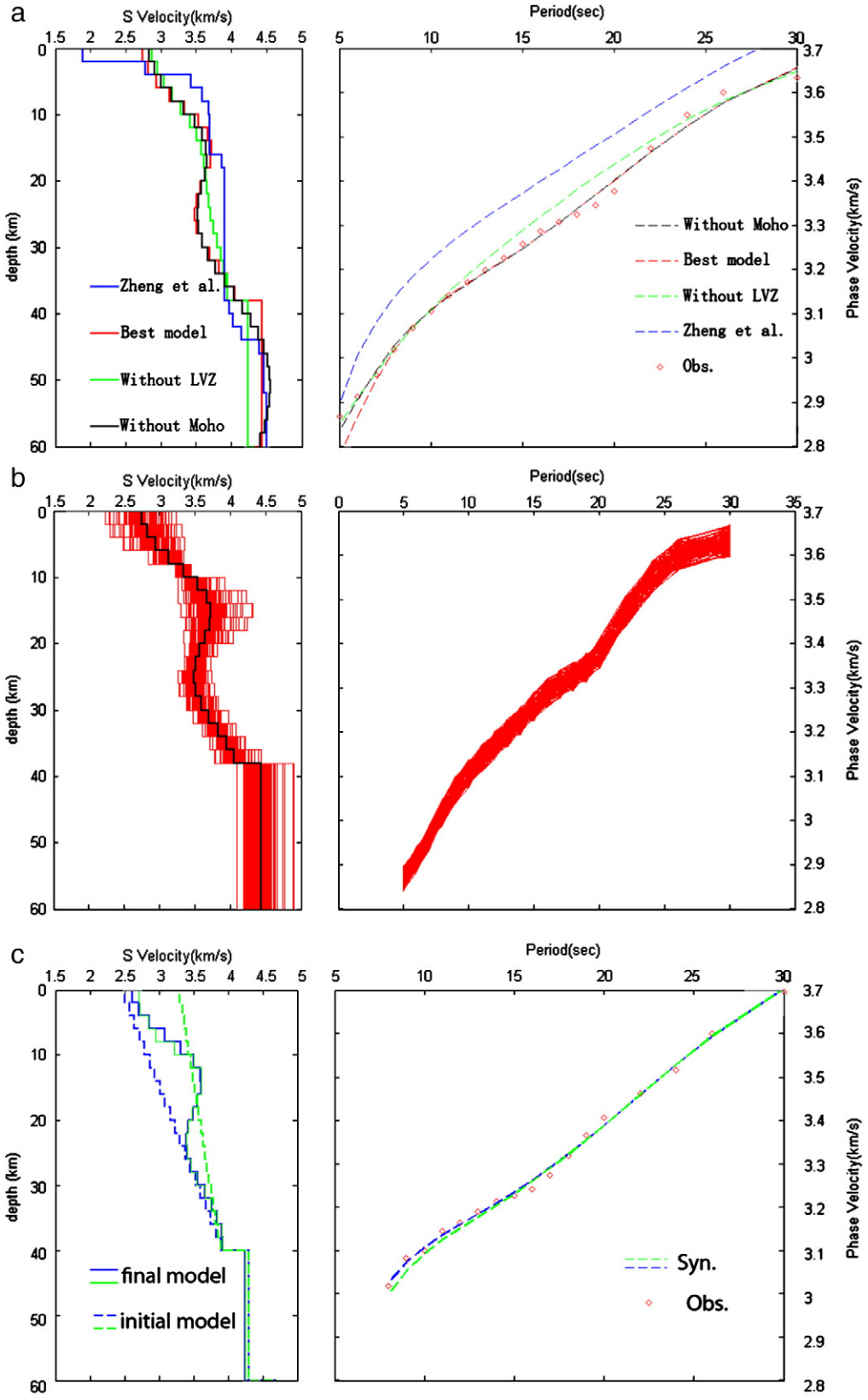

Fig. 7. Tests on the robustness of the middle-to-lower crustal low velocity zone. (a) Comparisons of different velocity models and Rayleigh wave dispersion curves for the station pair 307–308. The red diamonds denote the observations. In the left panel, the red line is the best fitting model, the black line is the model obtained with no initial Moho restriction, the green line represents a model without the LVZ, and the blue line is the result from waveform inversion of receiver functions (Zheng et al., 2009b). The dashed lines in the right panel are the dispersion curves calculated using the corresponding velocity models in the left panel. (b) A trial and error experiment for 307–308: 100 dispersion curves (in red) with 1% random noise added to the observed dispersion data (right panel) and the corresponding inversion results (left panel). The black line is the velocity model averaged over 100 obtained models (in red) after inversion. (c) An example of shear wave velocity inversion directly from inter-station dispersion measurements between stations 284 and 308. Dashed and solid lines in the left panel are the initial and inverted models, and red diamonds and lines in the right panel are the observed and synthetic dispersion curves from the inverted models, respectively.

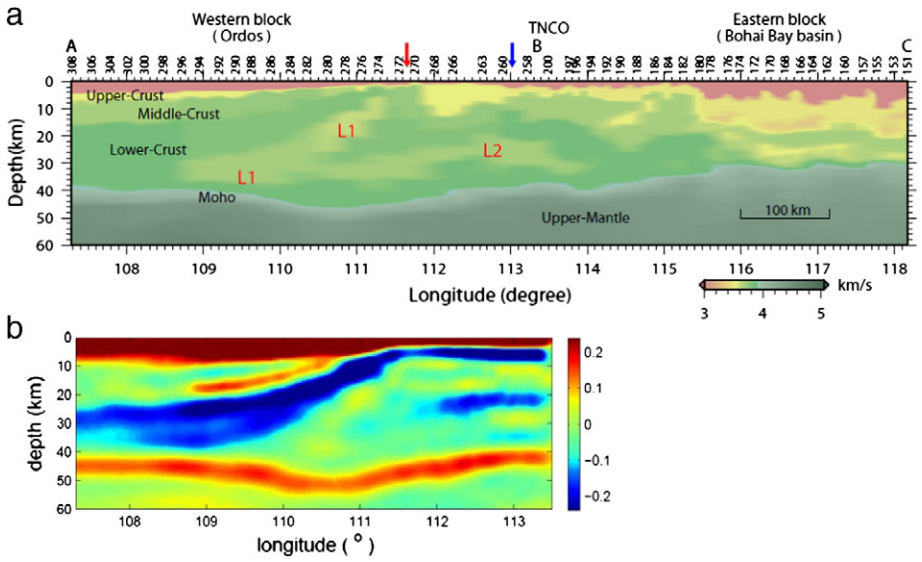

Fig. 8. (a) Shear wave velocity image under the two seismic arrays constructed by receiver function waveform inversion (Zheng et al., 2009b). L1 and L2 were proposed to be two large-scale low velocity zones in the crust. (b) Receiver function migration image under the NCISP-IV array modified from Chen et al. (2009). The strong negative signal extending to the western edge of the array and that in the middle crust under the eastern part of the array were interpreted to mark the upper interfaces of the two low velocity zones. (i.e., L1 and L2 shown in (a)).

shown in Fig. 9a) and radial anisotropy images (not shown) are essentially similar to those shown in Fig. 6, indicating that the inversions are stable and have converged to reliable solutions. We also evaluated the reliability of the anisotropic structure in different parts of the crust (0–10 km, 10–24 km and 24 km-Moho, respectively) by replacing each part of the inverted V_{SV} model with its V_{SH} counterpart with or without modifications and comparing the corresponding synthetic dispersion curves with the observation (Fig. 9b). It shows that the difference between the observed dispersion curve and that from an isotropic crust in the TNCO does require a strong positive radial anisotropy in the middle crust (10–24 km), even considering about 1% uncertainties of the data. Moreover, a rapid change in amplitude (even with a polarity reverse) of radial anisotropy from the middle crust to both the upper and lower crust is also demanded to explain the observed dispersion curves, although the amplitude of the radial anisotropy in the upper and lower crust is not stringently constrained as well (Fig. 9b). All these testing results confirm the robustness of the imaged structural feature beneath the TNCO (Fig. 6).

Compared with the receiver function images (Fig. 8), fine structures including the small-scale structure beneath the TNCO and the steepest part of the westward inclined LVZ in the eastern Ordos cannot be properly delineated from surface wave tomography (Fig. 6a and b), due largely to the relatively lower lateral resolution. Moreover, because of the better qualities and quantities of the Rayleigh phase velocity dispersion data than Love waves (Table 1 and Fig. 3), the V_{SV} structure is better resolved than the V_{SH} counterpart in our results (compare Fig. 6a with Fig. 6b). Therefore, the estimated crustal radial anisotropy may have uncertainties, especially at small values. In the later interpretation, we only consider relatively large values (>8%) of radial anisotropy, and focus on the lateral and vertical structural variations in the middle and lower crust.

5. Discussion

Our shear wave velocity images derived from ambient noise interferometry and surface wave phase velocity inversion (Fig. 6a and b) reveal great heterogeneities and systematic variations of the crustal velocity structure from east to west beneath the NCC, broadly consistent with previous receiver function studies using the same array data (Fig. 8, Zheng et al., 2009b; Chen et al., 2009). In particular, despite the relatively lower resolution, the better-resolved V_{SV} structure well resembles the shear velocity structure derived from receiver function waveform inversion (Zheng et al., 2009b). Both are featured by a much slower middle–lower crust beneath the eastern NCC, sharp structural change near the boundary between the eastern NCC and the TNCO, and distinct low velocity structures dominant in the middle to lower crust from the western margin of the TNCO to the western NCC (compare Fig. 6a with Fig. 8a). These comparisons attest to the robustness of the imaged structural features and hence the reliability of both results. Our study therefore provides a successful example of effective two-dimensional crustal structure imaging by applying ambient noise interferometry to linear seismic array data.

More importantly, the large-scale regional variations of crustal radial anisotropy obtained in this study are complementary to the structural information derived in the previous crustal studies. As mentioned before, the V_{SV} and V_{SH} referred in this study (Fig. 6a and b) represent velocities of shear waves propagating along the two seismic arrays with vertical and transverse polarization (normal to the array) directions, respectively. In this regard, our result of crustal radial anisotropy (Fig. 6c) may not be exactly the same as the commonly defined radial anisotropy—the difference in azimuth-averaged velocities of horizontally and vertically polarized shear waves (e.g., Shapiro et al., 2004; Huang et al., 2010; Moschetti et al., 2010). However, the good correlation among the imaged pattern of crustal radial anisotropy, other geophysical and geological observations and regional tectonics (see below) indicates that our results are viable in constraining the deformation especially in the middle and lower crust of the study region. A combination of the observations in this and previous studies therefore allows for a more comprehensive understanding of the structure and deformation of the crust in the NCC.

5.1. Bohai Bay Basin and Taihang Mountains (eastern and central NCC)

The most significant feature revealed by our imaging results is the strong positive middle-to-lower crustal radial anisotropy prevailing beneath the NCISP-II array, corresponding to areas affected by recent extensional tectonics, i.e., the Bohai Bay Basin in the eastern NCC and the Taihang Mountains in the TNCO (Fig. 6c). The eastern NCC has undergone significant crustal extension during the late Mesozoic to Cenozoic, as manifested by the widespread development of extensional

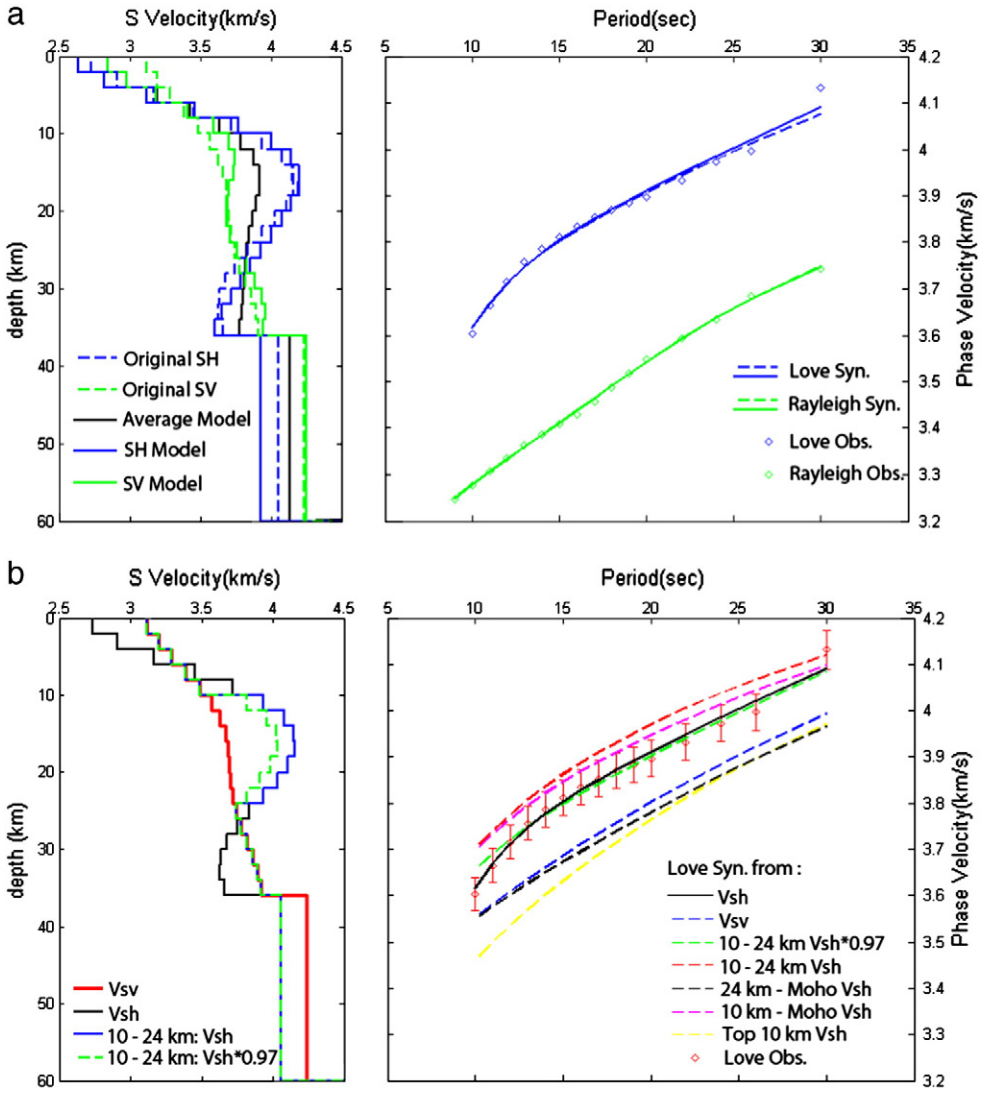

Fig. 9. Tests on the robustness of the imaged structure beneath the TNCO with examples for the station pair 190–191. (a) Re-inversion results with the average of the obtained V_{SH} and V_{SV} models as the initial model; (b) shear velocity models, constructed by considering the V_{SH} structure or its modified version in different parts of the V_{SV} model, and corresponding Love wave dispersion curves compared with the observations. Red bars stand for the ±1% uncertainties of the observed dispersion data.

structures, such as metamorphic core complexes (Liu et al., 2005; Yang et al., 2007a; Lin et al., 2008b) and large rifting basins including the Bohai Bay Basin (Ren et al., 2002). Bordering the eastern NCC in the west, the Taihang Mountains formed as an extensional orogen in the Late Mesozoic, and the evolution of the this mountain range was proposed to have been tectonically coupled with that of the Bohai Bay Basin to the east (Liu et al., 2000). Such a correlation between strong positive crustal radial anisotropy and predominant extensional tectonics is, in fact, not unique in the NCC, it has also been observed in many other extensional provinces, such as the Moldanubian terrane in the central European Variscan belt (Rabbel and Lueschen, 1996; Meissner et al., 2006), Basin and Range in the western United States (Moschetti et al., 2010), and extensional areas in the European Alps (Pohl et al., 1999) and Tibet (Shapiro et al., 2004; Huang et al., 2010). The similarities in the crustal radial anisotropy suggest that the crust in these extensional regions may have similar rheological properties and share a common regime of deformation.

We interpret the strong positive radial anisotropy beneath the Bohai Bay Basin and Taihang Mountains as a result from the sub-horizontal alignment of seismically anisotropic crustal minerals induced by the finite strains accompanying extension. Laboratory measurements and theoretical calculations have established that at middle to lower crustal depths seismic anisotropy can be a signature of ductile deformation and is primarily attributed to the lattice-preferred orientations (LPO) of major rock-forming minerals, in particular micas and amphiboles (Mainprice and Nicolas, 1989; Weiss et al., 1999; Nishizawa and Yoshitno, 2001). Most of these minerals typically show hexagonal symmetry with the orientation of axis of symmetry depending on strain orientation (Meissner et al., 2006). In the case of crustal extension, the associated shear strains preferentially orient the seismic slow axes (axis of symmetry) to the vertical direction (Mainprice and Nicolas, 1989), which explains the observations of strong positive radial anisotropy in the deep crust beneath the extensional regions in the NCC and many others worldwide.

Indeed, the pattern of radial anisotropy, low velocities and a thin crust beneath the Bohai Bay Basin inferred in this and previous seismic studies are qualitatively consistent with geological observations that widespread intracrustal ductile deformation took place in this region in response to the intensive extension during the cratonic destruction in the Late Mesozoic to early Cenozoic. Ductile deformation may have led to direct denudation of the middle–lower crust, resulting in

widespread development of metamorphic core complexes (Liu et al., 2005; Yang et al., 2007a; Lin et al., 2008b) and rifting and thinning of the crust (Ren et al., 2002). These crustal processes appear to have happened in association with intensive magmatism and a change in the nature and thickness of the lithospheric mantle in the eastern NCC, which eventually led to the present-day slow and thin crust with marked deep crustal radial anisotropy (Fig. 6) underlain by a thin (60–100 km), hot (~65 mW/m^2) and fertile lithosphere (Zhu et al., 2011 and references therein). All these observations suggest that the cratonic destruction in the eastern NCC may have involved the entire lithosphere vertically, with not only fundamental destruction of the lithospheric mantle but also marked modifications and thinning of the crust (mainly the middle to lower crust).

The comparable amplitudes and good westward continuity of the positive radial anisotropy in the middle crust of the Taihang Mountains suggest that this part of the crust may have been deformed in a same way accompanying the regional extension and cratonic destruction. The gradual elevation of the positive anisotropic anomaly from the lower crust in the eastern Bohai Bay Basin to the middle crust under the Taihang Mountains (Fig. 6c) was probably related to the Tertiary rifting and subsequent thermal subsidence in the east basin area and uplifting in the west mountain range (e.g., Liu et al., 2000; Ren et al., 2002). If this is the case, then the present-day eastward inclined positive anisotropic anomaly might be flat, even dip to the west in the Late Mesozoic. During that period of time, lithospheric extension and destruction may have been the most intensive (Wu et al., 2005; Zhu et al., 2011) and the geothermal gradient been higher (because of voluminous magmatism) and therefore the depth of ductile deformation been shallower in the eastern NCC than in the central NCC.

The Taihang Mountain region has a more complex pattern of crustal anisotropy than the Bohai Bay Basin, as indicated by a marked change in radial anisotropy from strong positive in the middle crust to weak-to-negative in the lower crust and around the Moho (Fig. 6c). This anisotropy pattern change corresponds to a westward thickening and relatively high Vp/Vs ratios of the crust (Fig. 10), and a thick crust–mantle transition zone up to 10 km constrained both petrologically and seismologically (Chen et al., 2001; Zheng et al., 2008). These structural features are consistent with previous suggestions that significant underplating of mantle-derived magma has taken place under the TNCO in the Phanerozoic, resulting in intensive crust–mantle interactions and reworking of the ancient lower crust (e.g., Zhou et al., 2002; Zheng et al., 2009a; Jiang and Guo, 2010).

We propose that the imaged weak to negative radial anisotropy in the lower to lowermost crust beneath the Taihang Mountains may be a record of crustal deformation associated with magma underplating in an extensional tectonic regime during the Phanerozoic evolution. Intrusion of mafic–ultramafic upper mantle minerals (e.g., olivine and orthopyroxene) during crustal assimilation by the underplated magmas (e.g., Zhou et al., 2002; Zheng et al., 2009a) may dilute and even change the type of anisotropy in the lower crust. This is because the fabric symmetry of these minerals (mostly orthorhombic) is different from typical crustal rocks and the measured anisotropy strongly depends on the direction of shear wave propagation relative to the crystallographic fabric (LPO) of the minerals (e.g., Kern, 1993; Barruol and Kern, 1996). In our case that shear waves propagate sub-parallel to the crustal extension direction (ductile flow direction) (Fig. 1), olivine-bearing mafic–ultramafic rocks are expected to show little radial anisotropy, which explains at least partially the rapid amplitude reduction of positive radial anisotropy in the lower crust under the Taihang Mountains (Fig. 6c). Considering the different but complex anisotropic behavior of plagioclase compared to micas and amphibole (Mainprice and Nicolas, 1989; Siegesmund and Kruhl, 1991), it is also possible that plagioclase-rich granulites as the cumulate from magmas by crustal anatexis during underplating (Jiang and Guo, 2010) may also contribute (albeit with larger uncertainties) to the observed weak to negative radial anisotropy in this region.

The detected vertical change in crustal radial anisotropy (Fig. 6c) and the fine-scale structural variations inferred previously beneath the Taihang Mountains (Fig. 8a, Zheng et al., 2009b) indicate that this region may have experienced crustal complex deformation and modifications compared with the Bohai Bay Basin to the east. Combined with the highly variable lithospheric structure (e.g., Chen et al., 2009; Zhao et al., 2009; Chen, 2010) and marked isotopic and chemical heterogeneities of mantle xenoliths in the TNCO (e.g., Tang et al., 2006; Xu, 2007), this strongly suggests that the Mesozoic–Cenozoic lithospheric reactivation may have affected the central NCC but spatially unevenly on both the crust and lithospheric mantle.

5.2. Ordos Basin (western NCC)

Unlike the eastern NCC and TNCO, the crust of the western NCC is featured by relatively long-wavelength structures, larger thickness and overall weak radial anisotropy (Figs. 6 and 8). The crustal structural features probably reflect weak crustal deformation and modifications, in agreement with the long-term tectonic stability of the region.

The most striking long-wavelength structure delineated seismically is the LVZ lying in the middle to lower crust of the Ordos Basin. Based on the velocities and shape of the LVZ imaged from waveform inversion of receiver functions (L1 in Fig. 8a), Zheng et al. (2009b) and Zhu and Zheng (2009) interpreted it as a remnant of upper–middle continental crust subducted beneath the eastern to middle part of the Ordos during the final assembly of the eastern and western NCC at ~1.85 Ga (Zhao et al., 2005). However, the imaging results from our surface wave tomography (Fig. 6a), previous receiver function wave-equation migration (Fig. 8b, Chen et al., 2009) and a new P wave free surface reverberations study (Chen et al., in preparation) all suggest that the LVZ is present under the entire Ordos Basin along the NCISP-IV array, with a nearly flat geometry over a major part of the region (dip<3°). A strong middle-to-lower crustal discontinuity, probably the upper interface of the LVZ, was also imaged by receiver function migration to cross the entire Ordos with a similarly low dip along an E–W profile some 400 km to the south of the NCISP-IV array (Chen et al., in preparation). These observations probably indicate that the deep-crustal LVZ is a common structure beneath the Ordos region. The nearly flat geometry of the LVZ appears to be in concordance with the gentle monoclinal structure with a 1–2° dip to the west of the sedimentary strata in the basin (except obvious uplift and depression developed at the margins) (e.g., Liu et al., 2006; Yang et al., 2009; Jiao et al., 2011). This indicates that the westward inclination of the LVZ may not be a signature of continental subduction during the Paleoproterozoic assembly of the NCC, but probably resulted from the tilting to the west of the whole Ordos Basin in the Phanerozoic that eventually led to the formation of the present-day huge monoclinal structure of the basin (e.g., Deng et al., 2005). The preservation of the LVZ under the entire Ordos suggests that the LVZ itself may represent an ancient structure that developed before the Phanerozoic tilting and have been preserved in the deep crust of the stable Ordos over a long span of geological time. The cause(s) and means of survival of this large-scale LVZ have been certainly closely associated with the tectonic evolution of the Ordos Basin as a whole and its surroundings, and therefore are interesting topics for further investigations.

In contrast to the regional coverage of the LVZ, the other specific structural feature of the Ordos Basin highlighted in this study is of local scale, i.e., the presence of obvious positive radial anisotropy locally in the lower crust (Fig. 6c). This is a rather intriguing feature, because it is spatially coincident with the area featured by a local crustal thickening uncorrelated with topography, an increase in average crustal Vp/Vs ratio, a thick and probably denser crust–mantle transition zone (Wei et al., 2011), an abrupt increase in the magnitude of upper mantle azimuthal anisotropy (deformation) (Zhao et al., 2008) (Fig. 10), and also the most rapid change in the lithospheric thickness (>100 km over a lateral distance of ~200 km) over the region (Chen et al., 2009).

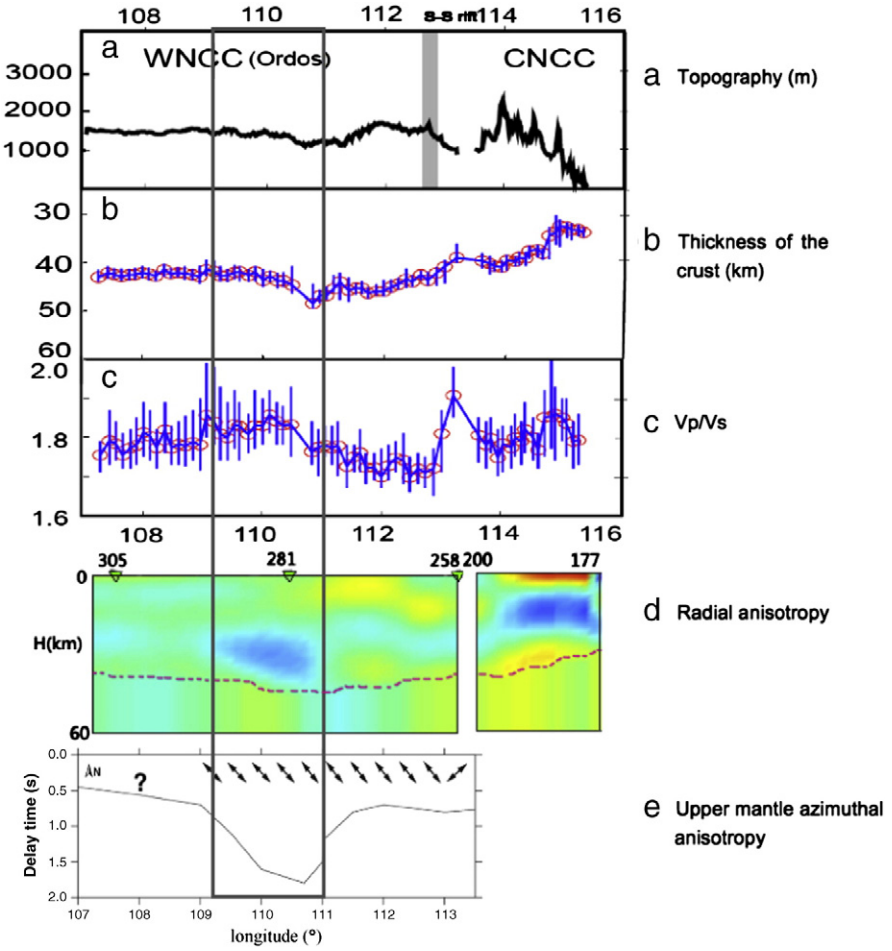

Fig. 10. Comparison of the topography (a), thickness (b) and Vp/Vs ratio (c) of the crust (Wei et al., 2011), radial anisotropy (d) and upper mantle azimuthal anisotropy (Zhao et al., 2008) beneath the WNCC array (e). (d) is the same as the corresponding part shown in Fig. 6c. In (e), arrows denote fast direction beneath the profile with respect to north; solid line represents delay time; symbol "?" indicates the region where uncertainty of the fast direction exists.

Detailed comparisons show that this localized lower-crust structure anomaly shares some common features with that beneath the Taihang Mountains in the TNCO, including the apparently thickened crust, gradual crust–mantle transition and relatively high Vp/Vs ratios of the crust. Comparably, these features suggest that the lower crustal anomaly under the Ordos Basin may also reflect crustal deformation associated with magmatic underplating/invasion, and be contributed mainly from the deformation fabrics of intruded mafic–ultramafic anisotropic minerals, mostly olivine. The discrepancy in the observed radial anisotropy in the two areas may be due to the different amounts of intrusions and different relations between the propagating direction of shear waves considered here and the LPO (a-axis) of the olivine: sub-parallel with each other in the Taihang Mountains as mentioned before (Fig. 1) and oblique by ~50° in the Ordos Basin (Fig. 10e). The a-axis of olivine in the lower crust under the Ordos Basin is tentatively assumed to be parallel to that of the upper mantle (flow direction)—typically the fast shear wave polarization direction from SKS splitting measurements (Fig. 10e). We made such an assumption by considering the good correspondence between the positive lower-crustal radial anisotropy and the strong azimuthal anisotropy in the upper mantle. We think it is reasonable also because experiment data suggest that high positive values of radial anisotropy can be expected when the shear waves propagate obliquely to the a-axis of olivine (with the highest values measured at 45°) (Kern, 1993), which well explains our observations in the Ordos region. If this interpretation is correct, our result combined with SKS splitting measurements would indicate that the lower crust and upper mantle under the Ordos Basin might have been deformed locally and probably in a coupled manner.

The observed coincident structural change is around the boundary between the Ordos Basin and the Cenozoic Yinchuan-Hetao rift area, and likely reflects the difference in the lithospheric structure between the stable Ordos and the surrounding tectonically active zones (Chen, 2010; Zhu et al., 2011). Through detailed structural comparisons at various depths in combination with surface geology and regional tectonics, Chen (2010) and Zhu et al. (2011) suggested that the distinct structural change may be a combined result of inherent lithospheric heterogeneities and repeated reactivation and modifications at pre-existing weak zones by successive thermal-tectonic events during the long-term evolution of the NCC. New petrological and geochemical data also provide evidence for intensive tectonics, magmatism and metamorphism that may have deformed and modified the structure and properties of the lithosphere at the boundary and adjacent areas of the Ordos in the Paleoproterozoic (e.g., Peng et al., 2010; Santosh et al., 2011; Yin et al., 2011), Paleozoic (e.g., Zhang et al., 2009, 2010), Mesozoic (e.g., Zhou et al., 2002; Zhang et al., 2009; Jiang and Guo, 2010), and even Cenozoic (Tang et al., 2006; Zheng et al., 2009a). However, the preservation of the regional-scale intracrustal LVZ even above the obviously deformed lower crust and upper mantle and the overall weak crustal deformation (Figs. 6, 8 and 10) indicate that the crust near the weak zones surrounding the stable Ordos may have not been much influenced albeit the lithosphere has been significantly thinned by multiple thermal-tectonic events (Chen et al., 2009). Based on the imaging results of this and previous studies, we therefore propose that the modification of the cratonic lithosphere at the boundary areas of the western NCC is probably a "bottom–up" process, which has not involved the crust noticeably.

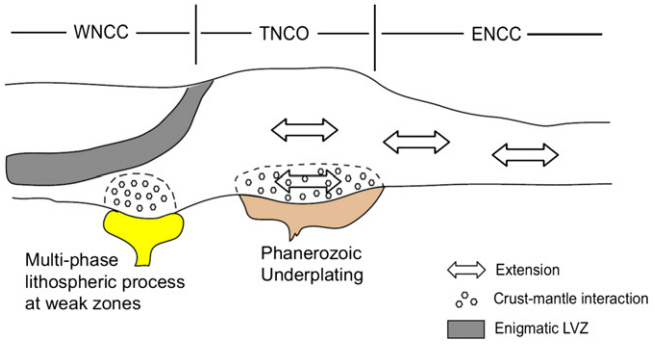

Fig. 11. A cartoon showing crustal modifications in the NCC implied by this study. See the main text for details.

6. Conclusion

We constructed two-dimensional images of crustal shear wave velocity and radial anisotropy by applying ambient noise interferometry and surface wave phase velocity inversion to the continuous data collected at two dense linear seismic arrays across the NCC. A combination of our images with other seismic observations, geological, petrographic and geochemical data enables a better understanding of the regional variations of the crustal structure and deformation associated with the cratonic lithospheric modification and destruction in the NCC. Our results show that the shear velocity structure and radial anisotropy pattern of the crust vary systematically among the three constituent parts of the NCC, in accordance with regional geology and tectonics (Fig. 11).

The eastern NCC is presently underlain by a slow and thin crust with predominant positive radial anisotropy in the middle to lower crust. This feature reflects marked modifications, thinning and extensional deformation of the crust, mainly the middle–lower crust, accompanying the fundamental destruction of the lithospheric mantle in the late Mesozoic to Cenozoic time.

The crust under the central NCC exhibits smaller-scale velocity variations and distinct changes in radial anisotropy from strong positive in the middle crust to weak-to-negative in the lower crust. The structural features suggest complex deformation and modifications of the crust probably associated with both tectonic extension and magmatic underplating during the Mesozoic–Cenozoic uneven lithospheric reactivation and modification.

A cratonic crust, characterized by a large-scale undisturbed intracrustal LVZ and weak deformation, is largely preserved under the western NCC albeit the lower crust has been locally deformed. Modifications of the cratonic lithosphere in this region may have been confined mainly in the lithospheric mantle at the boundary weak zones with relatively minor effects on the crust.

Acknowledgments

We thank the Seismic Array Laboratory in the Institute of Geology and Geophysics, Chinese Academy of Sciences for providing the seismic data and Professor Robert Herrmann of Saint Louis University for his Computer Programs in Seismology (CPS) software package. We are grateful to Tianyu Zheng and Zigen Wei for providing the receiver function imaging results of the crustal structure, Liang Zhao for SKS splitting measurements, Peng Peng and Jinghui Guo for thoughtful discussions on the regional geology. Constructive reviews from Yingjie Yang and an anonymous reviewer greatly improved the manuscript. This research is supported by the National Science Foundation of China (Grants 90814002 and 90914011) and Project SinoProbe-02-03.

References

Bao, X.W., Xu, M.J., Wang, L.S., Mi, N., Yu, D.Y., Li, H., 2011. Lithospheric structure of the Ordos Block and its boundary areas inferred from Rayleigh wave dispersion. Tectonophysics 499, 132–141.
Barruol, G., Kern, H., 1996. Seismic anisotropy and shear wave splitting in lower-crustal and upper-mantle rocks from the Ivrea Zone — experiments and calculated data. Physics of the Earth and Planetary Interiors 95, 175–194.
Bensen, G.D., Ritzwoller, M.H., Barmin, M.P., Levshin, A.L., Lin, F., Moschetti, M.P., Shapiro, N.M., Yang, Y., 2007. Processing seismic ambient noise data to obtain reliable broad-band surface wave dispersion measurements. Geophysical Journal International 169, 1239–1260.
Bensen, G.D., Ritzwoller, M.H., Shapiro, N.M., 2008. Broad-band ambient noise surface wave tomography across the United States. Journal of Geophysical Research 113, B05306. doi:10.1029/2007JB005248.
Carlson, R.W., Pearson, D.G., James, D.E., 2005. Physical, chemical, and chronological characteristics of continental mantle. Reviews of Geophysics 43 2004RG000156.
Chen, L., 2010. Concordant structural variations from the surface to the base of the upper mantle in the North China Craton and its tectonic implications. Lithos 120, 96–115.
Chen, S.H., O'Reilly, S.Y., Zhou, X.H., Griffin, W.L., Zhang, G.H., Sun, M., Feng, J.L., Zhang, M., 2001. Thermal and petrological structure of the lithosphere beneath Hannuoba, Sino-Korean Craton, China: evidence from xenoliths. Lithos 56, 267–301.
Chen, L., Wang, T., Zhao, L., Zheng, T.Y., 2008. Distinct lateral variation of lithospheric thickness in the northeastern North China Craton. Earth and Planetary Science Letters 267, 56–68.
Chen, L., Cheng, C., Wei, Z.G., 2009. Seismic evidence for significant lateral variations in lithospheric thickness beneath the central and western North China Craton. Earth and Planetary Science Letters 286, 171–183.
Chen, L. et al., in preparation. A sharp intra-crustal discontinuity with a velocity decrease beneath the stable Ordos plateau in North China.
Deng, J., Wang, Q.-f., Huang, D.-h., Gao, B.F., Yang, L.Q., 2005. Basement evolution of the Ordos Basin and its constraint on cap rock. Earth Science Frontiers 12 (3), 91–99 (in Chinese with English abstract).
Deng, J.F., Su, S.G., Niu, Y.L., Liu, C., Zhao, G.C., Zhao, X.G., Zhou, S., Wu, Z.X., 2007. A possible model for the lithospheric thinning of North China Craton: Evidence from the Yanshanian (Jura-Cretaceous) magmatism and tectonism. Lithos 96, 22–35.
Gao, S., Rudnick, R.L., Yuan, H.L., 2004. Recycling lower continental crust in the North China craton. Nature 432, 892–897.
Griffin, W.L., Zhang, A., O'Reilly, S.Y., Ryan, C.G., 1998. Phanerozoic evolution of lithosphere beneath the Sino-Korean craton. Mantle Dynamic and Plate Interactions in East Asia. Geodynamics 27, 107–126 AGU.
Herrmann, R.B., Ammon, C.J., 2004. Surface waves, receiver functions and crustal structure. Computer Programs in Seismology, Version 3.30. Saint Louis Universityhttp://www.eas.slu.edu/People/RBHerrmann/CPS330.html.
Huang, H., Yao, H.J., van der Hilst, R., 2010. Radial anisotropy in the crust of SE Tibet and SW China from ambient noise interferometry. Geophysical Research Letters 37, L21310. doi:10.1029/2010GL044981.
Jiang, N., Guo, J.H., 2010. Hannuoba intermediate-mafic granulite xenoliths revisited: assessment of a Mesozoic underplating model. Earth and Planetary Science Letters 293, 277–288.
Jiao, Z., Surdam, R.C., Zhou, L., Stauffer, P.H., Luo, T., 2011. A feasibility study of geological CO2 sequestration in the Ordos Basin, China. Energy Procedia 4, 5982–5989.
Kern, H.M., 1993. P- and S-wave anisotropy and shear-wave splitting at pressure and temperature in possible mantle rocks and their relation to the rock fabric. Physics of the Earth and Planetary Interiors 78, 245–256.
Li, S., Mooney, W.D., Fan, J.C., 2006. Crustal structure of mainland China from deep seismic sounding data. Tectonophysics 420, 239–252.
Li, S., Lai, X., Liu, B., Wang, Z., He, J., Sun, Y., 2011. Differences in lithospheric structures between two sides of Taihang Mountain obtained from the Zhucheng-Yichuan deep seismic sounding profile. Science China-Earth Sciences 54 (6), 871–880.
Lin, F.-C., Moschetti, M.P., Ritzwoller, M.H., 2008a. Surface wave tomography of the western United States from ambient seismic noise: Rayleigh and Love wave phase velocity maps. Geophysical Journal International 173, 281–298.
Lin, W., Faure, M., Patrick, M., Urs, S., Dominique, P., 2008b. Mesozoic extensional tectonics in Eastern margin of Eurasia continent, the Case study of South-Liaodong peninsula dome, NE China. Journal of Geology 116, 134–154.
Liu, D.Y., Nutman, A.P., Compston, W., Wu, J.S., Shen, Q.H., 1992. Remnants of 3800Ma crust in the Chinese part of the Sino-Korean craton. Geology 20, 339–342.
Liu, H.F., Liang, H.S., Li, X.Q., Yin, J.G., Zhu, D.F., Liu, L.Q., 2000. The Coupling Mechanisms of Mesozoic–Cenozoic Rift Basins and Extensional Mountain System in Eastern China. Earth Science of Geosciences 7, 477–486 (in Chinese).
Liu, J.L., Davis, A.G., Lin, Z.Y., Wu, F.Y., 2005. The Liaonan metamorphic core complex, Southeastern Liaoning Province, North China: a likely contributor to Cretaceous rotation of Eastern Liaoning, Korea and contiguous areas. Tectonophysics 407, 65–80.
Liu, C.Y., Zhao, H.G., Gui, X.J., Yue, L.P., Zhao, J.F., Wang, J.Q., 2006. Space–time coordinate of the evolution and reformation and mineralization response in Ordos Basin. Acta Geologica Sinica 80 (5), 617–638 (in Chinese with English abstract).
Mainprice, D., Nicolas, A., 1989. Development of shape and lattice preferred orientations: application to the seismic anisotropy of the lower crust. Journal of Structural Geology 11, 175–189.
Menzies, M.A., Fan, W.M., Zhang, M., 1993. Palaeozoic and Cenozoic lithoprobes and the loss of N120 km of Archaean lithosphere, Sino-Korean craton, China. In: Prichard, H.M., Alabaster, T., Harris, N.B.W., Neary, C.R. (Eds.), Magmatic Processes and Plate Tectonics. Geological Society Special Publication 76, 71–78.

Meissner, R., Rabbel, W., Kern, H., 2006. Seismic lamination and anisotropy of the Lower Continental Crust. Tectonophysics 416, 81–99.
Menzies, M., Xu, Y.G., Zhang, H.F., Fan, W.M., 2007. Integration of geology, geophysics and geochemistry: a key to understanding the North China Craton. Lithos 96 (1–2), 1–21.
Moschetti, M.P., Ritzwoller, M.H., Lin, F.C., Yang, Y.J., 2010. Seismic evidence for widespread western-US deep-crustal deformation caused by extension. Nature 464, 885–889.
Nishizawa, O., Yoshitno, T., 2001. Seismic velocity anisotropy in mica-rich rocks: an inclusion model. Geophysical Journal International 145, 19–32.
Peng, P., Guo, J.H., Zhai, M.G., Bleeker, W., 2010. Paleoproterozoic gabbronoritic and granitic magmatism in the northern margin of the North China craton: evidence of crust–mantle interaction. Precambrian Research 183, 635–659.
Pohl, M., Wenzel, F., Weiss, T., Siegesmund, S., Bohlen, T., Rabel, W., 1999. Realistic models of anisotropic laminated lower crust. Pure and Applied Geophysics 156, 139–156.
Rabbel, W., Lueschen, E., 1996. Shear wave anisotropy of laminated lower crust at the Urach geothermal anomaly. Tectonophysics 264, 219–234.
Ren, J.Y., Tamaki, K., Li, S.T., Zhang, J.X., 2002. Late Mesozoic and Cenozoic rifting and its dynamic setting in Eastern China and adjacent areas. Tectonophysics 344, 175–205.
Santosh, M., Liu, S.J., Tsunogae, T., Li, J.H., 2011. Paleoproterozoic ultrahigh-temperature granulites in the North China Craton: implications for tectonic models on extreme crustal metamorphism. Precambrian Research. doi:10.1016/j.precamres.2011.05.003.
Savage, M.K., 1998. Seismic anisotropy and mantle deformation: what have we learned from shear wave splitting? Reviews of Geophysics 37, 65–106.
Shapiro, N.M., Ritzwoller, M.H., Molnar, P., Levin, V., 2004. Thinning and flow of Tibetan crust constrained by seismic anisotropy. Science 305, 233–236. doi:10.1126/science.1098276.
Shapiro, N.M., Campillo, M., Stehly, L., Ritzwoller, M.H., 2005. High-resolution surface-wave tomography from ambient seismic noise. Science 307, 1615–1618.
Siegesmund, S., Kruhl, J.H., 1991. The effect of plagioclase textures on velocity anisotropy and shear wave splitting at deeper crustal levels. Tectonophysics 191, 147–154.
Tang, Y.J., Zhang, H.F., Ying, J.F., 2006. Asthenosphere–lithospheric mantle interaction in an extensional regime: implication from the geochemistry of Cenozoic basalts from Taihang Mountains, North China Craton. Chemical Geology 233, 309–327.
Teng, J.W., Wang, F.Y., Zhao, W.Z., Zhang, Y.Q., Zhang, X.K., Yan, Y.F., Zhao, J.R., Li, M., Yang, H., Zhang, H.S., Ruan, X.M., 2010. Velocity structure of layered block and deep dynamic process in the lithosphere beneath the Yinshan orogenic belt and Ordos Basin. Chinese Journal of Geophysics 53 (1), 67–85 (in Chinese).
Tian, X.B., Teng, J.W., Zhang, H., et al., 2011. Structure of crust and upper mantle beneath the Ordos Block and the Yinshan Mountains revealed by receiver function analysis. Physics of the Earth and Planetary Interiors 184, 186–193.
Wei, Z.G., Chen, L., Xu, W.W., 2011. Crustal thickness and Vp/Vs ratio of the central and western North China Craton and its tectonic implications. Geophysical Journal International 186, 385–389.
Weiss, T., Siegesmund, S., Rabbel, W., Bohlen, T., Pohl, M., 1999. Seismic velocities and anisotropy of the lower continental crust: a review. Pure and Applied Geophysics 156, 97–122. doi:10.1007/s000240050291.
Wu, F.Y., Lin, J.Q., Simon, A.W., Zhang, X.O., Yang, J.H., 2005. Nature and significance of the Early Cretaceous giant igneous event in eastern China. Earth and Planetary Science Letters 233, 103–119.
Wu, F.Y., Xu, Y.G., Gao, S., Zheng, J.M., 2008. Lithospheric thinning and destruction of the North China Craton. Acta Petrologica Sinica 24 (6), 1145–1174.
Xu, Y.G., 2007. Diachronous lithospheric thinning of the North China Craton and formation of the Daxin'anling–Taihangshan gravity lineament. Lithos 96, 281–298.
Xu, Y.G., Chung, S., Ma, J., Shi, L., 2004. Contrasting Cenozoic lithospheric evolution and architecture in the western and eastern Sino-Korean Craton: constraints from geochemistry of basalts and mantle xenoliths. Journal of Geology 112, 593–605.
Xu, Y.G., Lin, C.Y., Shi, L.B., Mercier, J.C., Ross, J.V., 1995. Upper mantle geotherm for eastern China and its geological implications. Science in China (Series B) 38, 1482–1492.
Yang, W.C., 1996. Theory and Methods of Geophysical Inversion. Geological Publishing House. (in Chinese).
Yang, J.H., Wu, F.Y., Chung, S.L., Lo, C.H., Wilde, S.A., Davis, G.A., 2007a. Rapid exhumation and cooling of the Liaonan metamorphic core complex: inferences from 40Ar/39Ar thermochronology and implications for Late Mesozoic extension in the eastern North China Craton. Geological Society of America Bulletin 119, 1405–1414.
Yang, Y.J., Ritzwoller, M.H., Levshin, A.L., Shapiro, N.M., 2007b. Ambient noise Rayleigh wave tomography across Europe. Geophysical Journal International 168, 259–274.
Yang, H., Fu, J.H., Wei, X.S., Ren, J.F., 2009. Tight sandstone gas reservoirs (exploration) in upper Paleozoic of Ordos Basin. 24th World Gas Conference (WGC2009), Buenos Aires, Argentina, Working Committee 1—Exploration and Production.
Yang, Y.J., Zheng, Y., Chen, J., Zhou, S.Y., Celyan, S., Sandvol, E., Tilmann, F., Priestley, K., Hearn, T.M., Ni, J.F., Brown, L.D., Ritzwoller, M.H., 2010. Rayleigh wave phase velocity maps of Tibet and the surrounding regions from ambient seismic noise tomography. Geochemistry Geophysics Geosystems 11, Q08010. doi:10.1029/2010GC003119.
Yao, H., van der Hilst, R.D., 2009. Analysis of ambient noise energy distribution and phase velocity bias in ambient noise tomography, with application to SE Tibet. Geophysical Journal International 179, 1113–1132.
Yao, H.J., Xu, G.M., Zhu, L.B., Xiao, X., 2005. Mantle structure from interstation Rayleigh wave dispersion and its tectonic implication in western China and neighboring regions. Physics of the Earth and Planetary Interiors 148, 9–54.
Yao, H.J., Van der Hilst, R.D., De Hoop, M.V., 2006. Surface-wave tomography in SE Tibet from ambient seismic noise and two-station analysis: I.—phase velocity maps. Geophysical Journal International 166, 732–744. doi:10.1111/j.1365-246X.2006.03028.x.
Yao, H.J., Beghein, C., Van der Hilst, R.D., 2008. Surface wave array tomography in SE Tibet from ambient seismic noise and two-station analysis: II. Crustal and upper-mantle structure. Geophysical Journal International 173, 205–219. doi:10.1111/j.1365-246X.2007.03696.x.
Yin, C.Q., Zhao, G.C., Guo, J.H., Sun, M., Xia, X.P., Zhou, X.W., Liu, C.H., 2011. U–Pb and Hf isotopic study of zircons of the Helanshan Complex: constrains on the evolution of the Khondalite Belt in the Western Block of the North China Craton. Lithos 122, 25–38.
Zhai, M., Santosh, M., 2011. The early Precambrian odyssey of the North China Craton: a synoptic overview. Gondwana Research 20, 6–25.
Zhang, Y.Q., Ma, Y.S., Yang, N., Shi, W., Dong, S.W., 2003. Cenozoic extensional stress evolution in North China. Journal of Geodynamics 36, 591–613.
Zhang, S.H., Zhao, Y., Liu, X.C., Liu, D.Y., Chen, F.K., Xie, L.W., Chen, H.H., 2009. Late Paleozoic to Early Mesozoic mafic–ultramafic complexes from the northern North China Block: constraints on the composition and evolution of the lithospheric mantle. Lithos 110, 229–246.
Zhang, X.H., Zhang, H.F., Jiang, N., Zhai, M.G., Zhang, Y.B., 2010. Early Devonian alkaline intrusive complex from the northern North China Craton: a petrologic monitor of post-collisional tectonics. Journal of the Geological Society of London 167, 717–730.
Zhang, H.F., Ying, J.F., Tang, Y.J., Li, X.H., Feng, C., Santosh, M., 2011a. Phanerozoic reactivation of the Archean North China Craton through episodic magmatism: evidence from zircon U–Pb geochronology and Hf isotopes from the Liaodong Peninsula. Gondwana Research 19, 446–459.
Zhang, Z.J., Yang, L.Q., Teng, J.W., Badal, J., 2011b. An overview of the earth crust under China. Earth-Science Reviews 104, 143–166.
Zhao, G.C., Wilde, S.A., Cawood, P.A., Sun, M., 2001. Archean blocks and their boundaries in the North China Craton: lithological, geochemical, structural and P–T path constraints and tectonic evolution. Precambrian Research 107 (1–2), 45–73.
Zhao, G.C., Sun, M., Wilde, S.A., Li, S., 2005. Late Archean to Paleoproterozoic evolution of the North China Craton: key issues revisited. Precambrian Research 136, 177–202.
Zhao, L., Zheng, T.Y., Lu, G., 2008. Insight into craton evolution: constraints from shear wave splitting in the North China Craton. Physics of the Earth and Planetary Interiors 168, 153–162.
Zhao, L., Allen, R.M., Zheng, T.Y., Hung, S.-H., 2009. Reactivation of an Archean craton: constraints from P- & S-wave tomography in North China. Geophysical Research Letters 36, L17306. doi:10.1029/2009GL039781.
Zheng, J., O'Reilly, S.Y., Griffin, W.L., Lu, F., Zhang, M., Pearson, N.J., 2001. Relict refractory mantle beneath the eastern North China block: significance for lithosphere evolution. Lithos 57, 43–66.
Zheng, J.P., Griffin, W.L., O'Reilly, S.Y., Lu, F.X., Wang, C.Y., Zhang, M., Wang, F.Z., Li, H.M., 2004. 3.6 Ga lower crust in central China: new evidence on the assembly of the North China Craton. Geology 32, 229–232.
Zheng, T.Y., Zhao, L., Zhu, R.X., 2008. Insight into the geodynamics of cratonic reactivation from seismic analysis of the crust–mantle boundary. Geophysical Research Letters 35, L08303. doi:10.1029/2008GL033439.
Zheng, J.P., Griffin, W.L., Qi, L., O'Reilly, S.Y., Sun, M., Zheng, S., Pearson, N., Gao, J.F., Yu, C.M., Su, Y.P., Tang, H.Y., Liu, Q.S., Wu, X.L., 2009a. Age and composition of granulite and pyroxenite xenoliths in Hannuoba basalts reflect Paleogene underplating beneath the North China Craton. Chemical Geology 264, 266–280.
Zheng, T.Y., Zhao, L., Zhu, R.X., 2009b. New evidence from seismic imaging for subduction during assembly of the North China craton. Geology 37, 395–398.
Zhou, X.H., Sun, M., Zhang, G.H., Chen, S.H., 2002. Continental crust and lithospheric mantle interaction beneath North China: isotopic evidence from granulite xenoliths in Hannuoba, Sino-Korean craton. Lithos 62, 111–124.
Zhu, R.X., Zheng, T.Y., 2009. Destruction geodynamics and Paleoproterozoic plate tectonics of the North China Craton. Chinese Science Bulletin 54 (19), 3354–3366.
Zhu, R.X., Chen, L., Wu, F.Y., Liu, J.L., 2011. Timing, scale and mechanism of the destruction of the North China Craton. Science China-Earth Sciences 54 (6), 789–797.